A&A 472, 705–713 (2007)
DOI: 10.1051/0004-6361:20067040

Astronomy & Astrophysics

The *Beppo*SAX WFC X-ray source catalogue[⋆]

F. Verrecchia[1], J. J. M. in 't Zand[2], P. Giommi[1], P. Santolamazza[1], S. Granata[1], J. J. Schuurmans[2], and L. A. Antonelli[1,3]

[1] ASI Science Data Center (*ASDC*), c/o ESA-ESRIN, via Galileo Galilei, 00044 Frascati, Rome, Italy
e-mail: `verrecchia@asdc.asi.it`
[2] Netherlands Institute for Space Reasearch (*SRON*), Sorbonnelaan 2, 3584, CA Utrecht, The Netherlands
[3] INAF – Osservatorio Astronomico di Roma (*OAR*), via Frascati 33, Monteporzio Catone, Rome, Italy

Received 28 December 2006 / Accepted 26 June 2007

ABSTRACT

Aims. We present the catalogue of X-ray sources detected by the two Wide Field Cameras (WFCs) in complete observations on board *Beppo*SAX during its 6 years of operational lifetime, between April 1996 and April 2002.

Methods. The *Beppo*SAX WFCs were coded mask instruments sensitive in the 2–28 keV energy band with a 40×40 square degree fields of view, pointing in opposite directions and perpendicularly to the *Beppo*SAX Narrow Field Instruments (NFI). The WFCs were usually operated simultaneously to NFI observations, each lasting up to several days. WFCs observed thus the entire sky several times with a typical sensitivity of 2 to 10 mCrab. A systematic analysis of all WFC observations in the *Beppo*SAX archive has been carried out using the latest post-mission release of the WFC analysis software and calibrations.

Results. The catalogue includes 253 distinct sources, obtained from a total sample of 8283 WFC detections. We describe the basic statistical properties of the sample and present a six-year history of two celestial calibration X-ray sources.

Key words. catalogs – X-rays: binaries – X-rays: galaxies – X-rays: general – X-rays: stars – Galaxy: general

1. Introduction

The *Beppo*SAX X-ray astronomy satellite (Boella et al. 1997), was a major program of the Italian Space Agency (ASI) with participation of the Netherlands Agency for Aereospace Programs (NIVR). The main scientific goal of the mission was to perform spectroscopic and timing studies of several classes of X-ray sources in a very broad energy band (0.1–300 keV). The satellite was launched on April 30, 1996 and observations were carried out until April 30, 2002.

The scientific payload comprised four Narrow Field Instruments (NFIs) and two Wide Field Cameras (WFCs) pointing in opposite directions from each other and perpendicular to the NFI (Boella et al. 1997; Jager et al. 1997). The WFC observations covered the whole sky multiple times over the period 1996–2002 (see Fig. 1).

The WFCs large field of view (FOV) and good sensitivity made these instruments suitable to detect and locate X-ray transient sources with a precision of a few arcminutes and to monitor large parts of the sky. Among the most important results obtained with the WFCs is the discovery of the X-ray afterglow phenomenon of Gamma Ray Bursts in 1997 (Costa et al. 1997). Moreover, the 12 monitoring campaigns of the Galactic Bulge allowed the spectral and timing monitoring of known persistent and transient X-ray sources and the discovery of many new galactic X-ray transients and phenomena (see for example Ubertini et al. 1999; Cornelisse et al. 2000; in 't Zand 2001, 2004a; Cornelisse et al. 2003). These observations resulted in a significant advance in the knowledge of the transient emission properties of low mass X-ray binaries (e.g., in 't Zand et al. 2004b,c).

After the end of the mission a systematic data analysis of the entire WFCs archive was carried out. This analysis, based on the processing of two complementary datasets, allowed us to build the complete catalogue of WFC X-ray sources and an archive of high-level data products, including energy spectra and light curves of the brighter sources. This archive is accessible on the web through the ASDC multi-mission interactive archive (`http://www.asdc.asi.it/mmia/`).

In this paper we present the final *Beppo*SAX WFC source catalogue including 253 distinct and previously known X-ray sources except for a new transient. The catalogue was obtained from a total sample of 8283 true detections.

This catalogue is the first complete all-sky survey above 2.5 keV since *HEAO-1 A4* (Levine et al. 1984) with 6 years of coverage corresponding to a net total exposure of over 100 million seconds and with a far better location accuracy. It contains more information on variability over long time scale in the hard X-ray band than for example the ROSAT all-sky survey catalogues, the ASCA 0.7–10 keV (Sugizaki et al. 2001) and the first three INTEGRAL-IBIS low galactic latitude surveys (Bird et al. 2004; Bird et al. 2006; Revnivtsev et al. 2004) and the high galactic latitude survey of the Swift-BAT (Markwardt et al. 2005), and comparable with the last INTEGRAL-IBIS survey (Bird et al. 2007).

2. Instrument and software description

2.1. General characteristics and the raw data archive

The WFCs were two identical coded mask instruments for the imaging of the hard X-ray sky (1.8–28 keV; Jager et al. 1997) developed and built by SRON. Their FOV was 40° × 40° each

---

[⋆] Table 3 is only available in electronic form at the CDS via anonymous ftp to `cdsarc.u-strasbg.fr(130.79.128.5)` or via `http://cdsweb.u-strasbg.fr/cgi-bin/qcat?J/A+A/472/705`

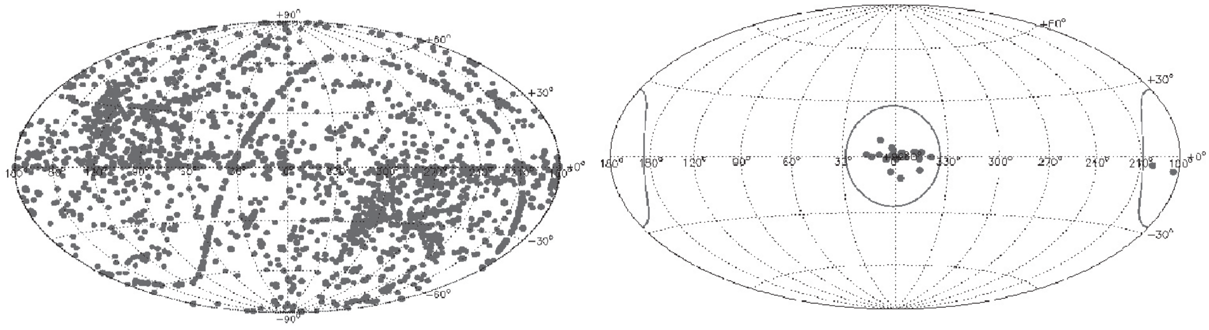

Fig. 1. The Aitoff projection in galactic coordinates of all the WFC observation pointing directions (*left*) and of the FOV of a typical WFC pointing of the Galactic Center (the circle includes the squared WFC FOV). WFC unit 1 points at Sgr-A and unit 2 at the anti-center, including the Crab Nebula.

(full width to zero response) with an angular resolution of 5′ (full width at half maximum, FWHM); the spectral and time resolution were 20% at 6 keV (FWHM) and 0.5 ms, respectively. The source location accuracy for bright sources (for the standard attitude reconstruction from star sensor data) was 1.4′ at 99% confidence level, and larger for less significant sources as measured through the signal-to-noise ratio (*SNR*). The on-axis sensitivity was in the range 2–10 mCrab for a typical *Beppo*SAX WFC observation of 3×10^4 s, and depended on the intensities of other sources in the same FOV.

These properties made the WFCs suitable instruments for the monitoring of medium to high intensity X-ray sources and for the study of transient X-ray phenomena.

The WFCs raw data archive has been stored in 2652 Final Observation Tapes (FOTs). FOTs corresponding to contiguous observing periods with the same pointing and roll angle, were combined to form a multi-FOT complete observation.

We carried out two data processing runs on two different data samples. The first pertains to all data when no part of the FOV is occulted by the Earth. Some FOTs were, thus, completely discarded and 1438 observations remained. The second sample pertains to all data (1543 observations), whether occulted by the Earth or not, and exposure corrections were applied for each source to take into account occultations. We performed two different processing runs because the first allowed a straightforward modelling of the detector background image resulting in less image artifacts, while the second allowed to obtain the longest source exposure to reduce statistical noise and increase source time coverage.

2.2. The WFC imaging algorithm

The WFCs are shadow mask cameras (Ables 1968; Dicke 1968). An opaque screen with a pseudo-random pattern of holes (coded mask) is placed in front of a position-sensitive detector (a multiwire proportional counter; Mels et al. 1988), so that X-ray sources in the FOV cast shadows on the detector, each displaced according to the off-axis position of the source. The WFC masks and detectors were of the same size and, therefore, only the on-axis position is fully coded with the mask pattern. However this configuration allows a better angular resolution at the same FOV compared to systems having the entire FOV fully coded.

The sky image is reconstructed with an iterative cleaning algorithm (“Iterative Removal Of Sources”, IROS; Hammersley 1986, Hammersley et al. 1992; in ’t Zand 1992), based on a cross-correlation of the detector image with the coded mask pattern (Fenimore & Cannon 1978). IROS performs a new cross-correlation during each iteration and new detections are localised via a fit with the expected Point Spread Function (PSF) and then compared to the positions of X-ray sources in a reference catalogue. Finally, each source that is significantly above the noise, is simulated on the detector plane, including its energy and angle-dependent spatial response, and then subtracted.

The main systematic error in the reconstructed sky is due to a residual spatial non-linearity in the detectors which cannot be accounted for. As a result physical pixel sizes are not completely identical and consequently the PSF shows inaccuracies. The main impact is on the sensitivity in very crowded FOVs for exposures longer than a few days (e.g., the Galactic Center field, hereafter GC) and on the source location accuracy which is hard limited to a best-case value of 1.4′ (99% confidence level; Heise et al. 1998).

2.3. The reference catalogue

The reference catalogue of X-ray sources used in the first data processing run includes 17674 entries. It was built combining various tables of known astronomical objects (see Table 1) in order to include a large sample of entries from extra-galactic catalogues to allow the detection of AGN and cluster of galaxies in the 2–10 keV band at a flux level near the limiting sensitivity. Each WFC FOV includes from a few hundred up to two thousand sources of the reference catalogue. This requires an adjustment of the detection threshold criteria since source positions are more likely to coincide with a noise peak when there are many “potential” sources in the FOV. In the second data processing run a smaller reference catalogue was used to reduce the probability of a coincidence of a known source with a noise peak. It was built by selecting sources with 1 keV flux density greater than 4.8×10^{-12} erg cm^{-2} s^{-1} keV^{-1} and including validated sources from the first processing run.

2.4. WFC processing procedure

Raw data consist of a list of events labelled with detector position, energy channel and detection time. Fluxes and positions of sources detected in an observation are determined from the raw data in three main steps (Jager et al. 1997):

- *I*: a “cleaned” event list is obtained from each FOT for time intervals with known and stable attitude, excluding all unwanted periods (such as those due to abnormal values of housekeeping parameters and passages through the South Atlantic Geomagnetic Anomaly). In the first processing run times were selected to keep the Earth outside the FOV, while

Table 1. The astronomical databases used to build the reference catalogue. Database acronyms, objects class and the references for each catalogue are shown from left to right. GC and GP are the Galactic Center and Plane.

Database name	Objects class	References
XRB	X-ray binary systems	van Paradijs (1995)
HMXRB	High mass X-ray binary systems	Liu et al. (2000)
LMXRB	Low mass X-ray binary systems	Liu et al. (2001)
INTEGRAL-IBIS GP soft γ-ray catalogue	X-ray binary systems	Bird et al. (2004)
INTEGRAL-IBIS hard X-ray GC survey		Revnivtsev et al. (2004)
Swift-BAT high galactic latitude survey	AGN	Markwardt et al. (2005)
ZCAT	galaxies with B magnitude <14	Huchra et al. (1992)
AGN	Active galactic nuclei	Padovani et al. (1997) and private communication
RASS-BSC	ROSAT all-sky survey bright sources with 0.1–2.4 keV flux > 10^{-11} erg s^{-1} cm^{-2}	Voges et al. (1999)
Sedentary	high energy peaked BL LACs (HBL)	Giommi et al. (1999), Giommi et al. (2005)
CABSCAT	Spectroscopic binary systems	Strassmeier et al. (1988), Strassmeier et al. (1993)
CVCAT	Cataclismic variable stars	Downes & Shara (1993)
ALLWARPS	Cluster of galaxies	Perlman et al. (2002)
BASSANI	Absorbed active galactic nuclei	private communication

in the second one periods were included when the Earth is inside the FOV (determining for each source the exposure when it is not occulted). Event lists from each FOT in a complete observation are merged;

- *II*: data products such as detector and sky images, and fluxes in specific energy bands are generated from event lists through the decoding process. A first decoding run is executed in the most sensitive band (i.e. ~2–8 keV, assuming a Crab-like spectrum), to select significant sources. Then the decoding algorithm is executed in all energy bands for these sources. In the second processing run a further decoding test in the 8–19 keV band was added to search for hard transient sources;
- *III*: higher level scientific products, such as spectral fits with simple models, spectral energy distributions and light curves are generated in the same bands for each detected source, applying *SNR* acceptance thresholds of 4.5 and 6.5 for sparse and crowded fields respectively.

The *SNR* is calculated by the WFC software using as noise the standard deviation evaluated on source plus background counts. This is because for the most part of sources the standard deviation is background dominated. Thresholds were preliminarly defined taking into account the large reference catalogue and the sensitivity dependence on the combined intensity of all sources in the FOV (see detailed description in Sect. 3.3).

At the end of the standard procedure, a visual inspection of the scientific products (spectra and light curves) was performed.

3. Results

In this section we describe how the fluxes were validated with data of well-documented stable X-ray sources and how the WFC catalogue was built through the creation of the final sample of detections.

3.1. The observations of the Crab Nebula and Cas A

As validation of both the WFC software and the standard analysis procedure at high, medium and low flux levels, we checked all the observations of a sample of well-documented stable X-ray sources including the Crab Nebula, Cas A and the Tycho supernova remnant. We show here some results for the Crab and Cas A from the first data processing run.

We analyzed 130 observations of the Crab Nebula at off-axis angles lower than 21° and exposures ranging between 1.67 and 129.7 ks. We calculated the relative deviations from the Crab Nebula 2–10 keV mean flux (2.12×10^{-8} erg cm^{-2} s^{-1}, evaluated using the final WFC response matrices) and corrected fluxes for a residual linear trend with off-axis angle between FOV center and borders of about 7%. This trend is mainly due to the decrease with the cosine of the angle of the number of photons detected per square cm. We plotted then the resulting 2–10 keV secular light curve of Crab Nebula (Fig. 2). A systematic error of about 2% was added in quadrature to the flux errors to make the data consistent with an expected reduced chi-square of 1. This error was applied to all the detections in the catalogue. We show in the bottom panel of Fig. 2 the Cas A corrected secular light curve obtained from 144 observations, compatible with a residual dispersion of ~6.2%. This dispersion is larger than the Crab one at the lower flux level of Cas A. A further systematic error of about 4.1% is needed to obtain again a reduced chi-square of 1. This term has not been added to flux errors.

3.2. Source identifications

Sources in the reference catalogue (see Sect. 2.3) were automatically identified by the IROS algorithm and then double-checked visually. Sources not identified or misidentified in the reference catalogue were cross checked with literature regarding sources discovered by ASCA, RXTE, *Beppo*SAX, INTEGRAL, Swift-BAT, XMM (for example see Sugizaki et al. 2001; Giommi et al. 2000; Bird et al. 2006, 2007; Markwardt et al. 2005, XMM-SSC 2003, 2006). Moreover we checked and updated, when necessary, source classifications.

3.3. Source detection filtering

The sensitivity at a certain position in the FOV depends on the off-axis angle (due to a dependence on effective area), on the particle-induced and cosmic diffuse backgrounds and on the combined intensity of all X-ray point sources in the FOV. The first three components are rather stable under nominal conditions, the latter varies considerably with galactic coordinates (the variations of the cosmic background above 2 keV are much smaller; see for example Kushino et al. 2002 and Lump et al. 2002). The largest concentration of bright X-ray sources is close

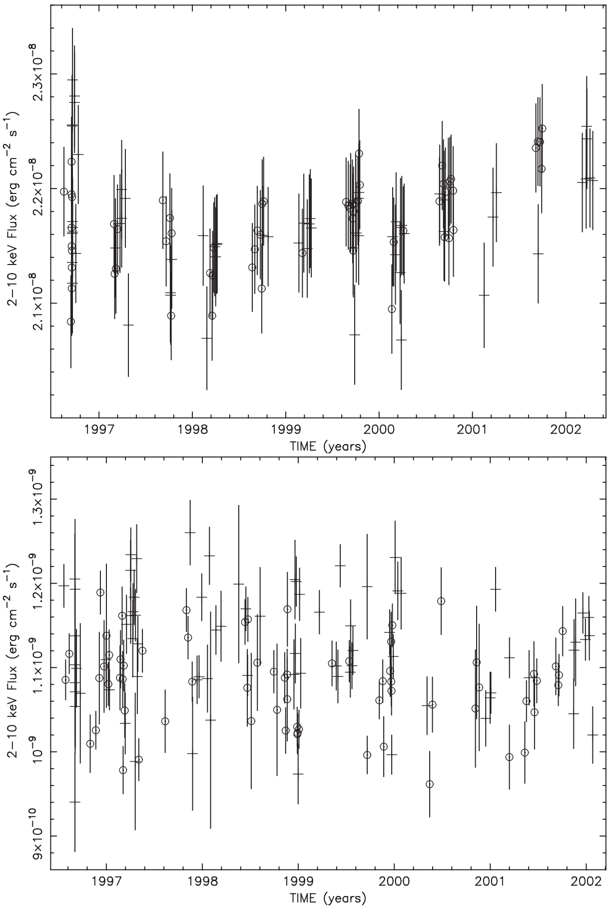

Fig. 2. The 2–10 keV Crab Nebula (*top panel*) and Cas A secular light curves corrected for the linear decrease with off-axis angle described in the text (open circles correspond to unit 1). A systematic error of ~2% was added in quadrature to the corrected flux errors for both WFCs to reach a reduced chi-square of ~1. Residual dispersions for corrected light curves are 2% and 6.2% respectively.

to the GC, where consequently the sensitivity is worse than elsewhere in the sky.

In fields crowded with bright sources there is a complicating factor related to a non-optimum imaging by the detectors. The detectors suffer from a differential non-linearity (Jager et al. 1997). Due to the dependence on the spectrum and off-axis angles of all detected sources, it is not completely accounted for in the IROS algorithm. The effect is so strong that a systematic sensitivity limit is reached for GC fields for an exposure longer than a few hundred ks.

In order to distinguish those fields where the contribution to the background from bright sources is dominant, we considered the Total Count Rate (hereafter TCR) of an observation. TCR is defined as the total number of events divided by the net exposure time. Using this parameter we selected observations of low background fields (TCR < 90 cts s^{-1} and TCR < 130 cts s^{-1} in the first and second data processing run respectively[1]), such as fields at high galactic latitude or those not crowded, and the high background ones at low latitude (TCR > 90, 130 cts s^{-1}).

The criterion to accept the detection of a point source is usually different between known and new sources. The acceptance threshold of a known source at a certain position is defined as the level of 3σ excess above the statistical noise induced at that position by all contributions mentioned above (where σ is the statistical standard deviation). This corresponds, for a Gaussian noise distribution, to a chance probability of less than 0.14%. Since in a coded aperture camera the flux for every position in the sky is reconstructed from photons on large portions of the detector, the noise distribution is still Gaussian.

In the case of a previously uncatalogued X-ray source, its position is not known so one needs to take into account the number of trials. This number is firstly determined from the number of independent pixels in the FOV, 255 × 255 (i.e., the WFC number of mask elements). If we require less than 1 false peak in 100 images, the threshold needs to be 5.3σ.

In our first procedure we implemented a very large reference catalogue, which produces in almost all WFC FOVs a large number of "potentially" visible known sources (see Sect. 2.3). This increases proportionally the probability for false detections (1000 potential sources in the FOV imply about 2 sources coincident by chance with 3σ excesses). This is not completely true however for GC fields, where the detectors non-linearity requires a fine tuning of the detection acceptance threshold.

In order to take into account all the factors and evaluate the required significance threshold, we built the cumulative distribution of all the 2–8 keV detection *SNR*s (Fig. 3) in both data processing runs. This plot is roughly similar to a "log *N*-log *S*" distribution.

We fit the data to a broken power law plus a cumulative Gaussian model (BPL + CG) and in Fig. 3 (left panel) we show both the components resulting from a fit to data from the first processing run stage (CG has a mean of 3.9 and $\sigma = 1.2$, while the BPL has slopes of ~–0.53, ~–0.01 and a break at $SNR \sim 4.0$). A BPL component was used to distinguish better the statistical noise component, represented by the CG component, from the true detections, represented by the BPL component. The BPL takes into account the instrumental sensitivity limits, the break roughly indicating the significance above which we can expect "true" detections following a power law distribution.

The CG component, describing the background noise distribution (both random and systematic), has parameters which imply a sample of ~4% of spurious detections at $SNR \geq 6.3$. We visually checked each marginal detection (with $SNR < 9$, a distance from the reference position greater than 5′ and at FOV borders). The percentage of discarded detections is ~2.8%, leaving about 1.2% of residual noise detections in the first processing run sample.

In Fig. 3 we also show the cumulative distributions for detections in three off-axis angle intervals, showing that the highest contribution to the CG noise component comes from detections at off-axis angles larger than 15° (~53% of all detections in the Gaussian component). These plots confirm the results of the visual inspection. Selecting detections with *SNR* greater than 6 from the first processing run, we obtained 7295 detections of 228 distinct sources.

In the right panel of Fig. 3 we show the 2–8 keV *SNR* cumulative curves for the second processing run. These curves show a much lower CG component in all curves, evident only for off-axis angles larger than 15°. It was very difficult to estimate this component from the total curve. However the estimated CG parameters (mean ~3.6 and $\sigma \sim 1.2$) ensure a contamination from spurious detections (~1% at *SNR* above 5.9) slightly larger than that obtained fitting the same component on the curve for

---

[1] In the second processing run sources have different net exposures, so we built this parameter using the shortest common exposure time among them. We verified these ranges of values using the "root mean squares" of significance images discussed below in this section, as an alternative test of a field background.

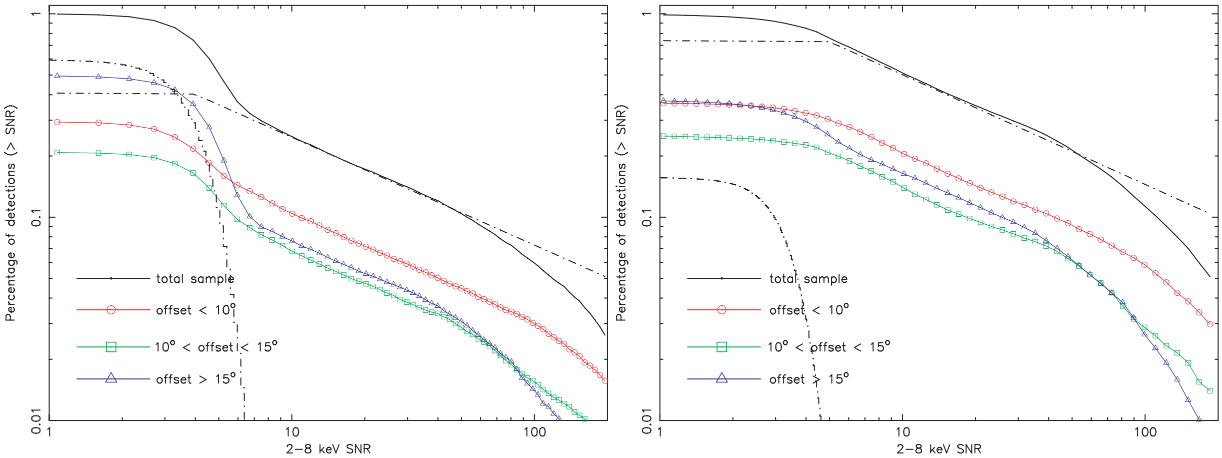

Fig. 3. The cumulative 2–8 keV *SNR* distributions of all the detections without any *SNR* cut for the first data processing run (*left panel*) and for the most complete one. The upper black thick curves are the total samples, the dash-dotted curves are the components of the fitted models (Gaussian + Broken power law, with parameters mean = 3.9, σ = 1.2, slopes ~–0.53 and ~–0.01 and break at ~4.0 for the first processing run and mean = 4.0, σ = 1.2, same slopes and break at ~5.8), while the remaining three lower curves are the distributions for different off-axis angle intervals (the circled one corresponds to off-axis angles <10°, the squared to 10–15 ° and the triangled to >15°).

off-axis angles larger than 15°. This lower CG component however confirms the effect of the reference catalogue on the first processing run.

In both processing runs the fitting process to the cumulative curves is not perfect. This is mainly due to the superposition of different noise components coming from different pointings (i.e., mainly from high/low background fields), but also to differences of all the other parameters which may influence the sensitivity among observations (such as different exposure times). Therefore, we first checked the *SNR* distributions for the low TCR sub-samples for both processing stages. We estimated a Gaussian component (mean ~3.0 and σ ~ 1.0) for the second stage which permits to establish a 1% contamination threshold in this curve at *SNR* = 4.8, while this component for the first processing run curve is comparable to that fitted on the total sample (threshold at 5.9).

As a final verification of the acceptability of low *SNR* (below *SNR* = 7) detections in low TCR fields, we computed specific 3σ confidence level thresholds for each field estimating their background noise standard deviation[2], and checked visually detections above these thresholds. Most of the low *SNR* detections in low background fields were discarded with this check, up to "single field" confidence levels of ~7σ.

We checked also results in harder bands from both processing runs, creating the same cumulative significance distributions (in Fig. 4 those relative to the second processing run). In particular for the 8–19 keV band we evaluated the CG component parameters (mean = 2.0 and σ = 2.7) using the same fit model, estimating a contribution of ~2.5% of noise detections above *SNR* = 7.

The catalogue has been obtained choosing detections from the second processing run having *SNR* > 6 if detected in the high TCR fields, or *SNR* > 5 if in the low ones. Finally we added to the catalogue a small sample of verified sources from the first processing run and not detected in the second one together with a sample of detections from harder bands. The complete sample of detections includes 8283 entries of 253 distinct sources.

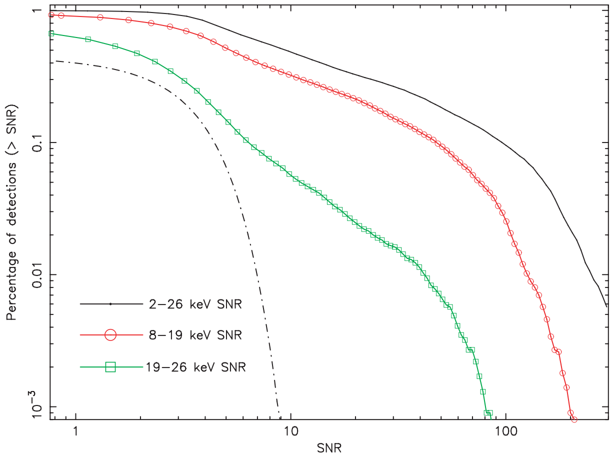

Fig. 4. The cumulative distributions of *SNR* in three larger/harder bands (2–26, 8–19, 19–26 keV) for detections of the second processing run. The Gaussian component of the model fitted to the 8–19 keV curve is shown.

4. The catalogue

The number of sources for the main classes of the 253 sources included in the catalogue are shown in Table 2. The positions and fluxes of the most significant detection of each source are reported in Table 3 (also available on-line at `http://www.asdc.asi.it/wfccat/`). At the end of the table a group of 11 rows includes sources detected in the first processing run only.

Table 3 gives as first column the *Beppo*SAX WFC designation (i.e., "SAXWFC"), followed by right ascension and declination (all celestial coordinates are for epoch J2000). In the following column the positional error is presented, which was calculated by a quadratic sum of the 1.3′ systematic uncertainty (see below) and the mean of the 99% confidence level errors in X and Y. Then are presented the source net exposure (in ks), the 2–10 keV flux and error (in erg cm^{-2} s^{-1}) for the maximum *SNR*

---

[2] We evaluated these thresholds on significance images (the ratio of the sky image to the poisson noise map from the first iteration of IROS), either calculating the "root mean square" of a complete image and of sub-images (85 × 85 pixels) around each source, or estimating directly the Gaussian background noise standard deviations. We corrected the 3σ levels for the number of potential sources in each FOV.

Table 2. Number of sources and detections for the main source classes in the WFC catalogue. The table does not include 37 detections of 2 X-ray pulsar sources, 4U 0142+614 and PSR J0540-6919.

Source class	Number of detections	Number of sources
candidate X-ray binaries	2	2
high Mass X-ray binaries	2045	49
low Mass X-ray binaries	4876	87
cataclismic variables	125	11
extended galactic sources	443	5
stars	99	21
white dwarfs	15	2
galaxies	14	2
AGN	472	45
cluster of galaxies	59	13
unclassified	96	14

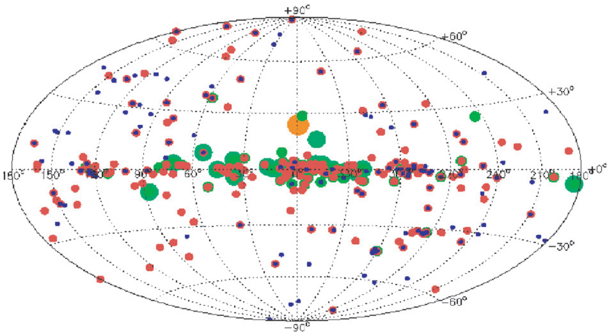

Fig. 5. The Aitoff projection of the *Beppo*SAX WFC detections: 8283 detections of 253 distinct X-ray sources in all the observations processed (symbol size is proportional to intensity).

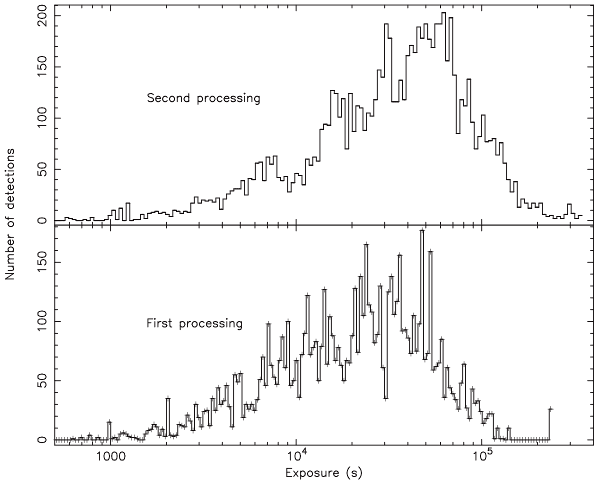

Fig. 6. The exposure distributions of the *Beppo*SAX WFC detections in all data processed.

detection, followed by the detection *SNR* in 2–8 and 8–19 keV bands. The number of detections and the total exposure of each source are in the ninth and tenth column. The mean flux and its error (in erg cm^{-2} s^{-1}), the reduced chi-square and the minimum and maximum flux among all the detections of a source are in columns from the eleventh to the fourteenth. The last two columns contain the source identification and the classification resulting from comparison with public databases.

Some statistical properties of the catalogue are hereafter described. The Aitoff projection in galactic coordinates of the full sample is shown in Fig. 5. The observation exposure distributions (Fig. 6) have a peak at ~30 ks and ~50 ks for the first and second processing stages respectively, while only a few long high galactic latitude and GC pointings have exposures up to 350 ks in the second processing run. The total exposure is ~67 Ms for the first processing run while the second one has a minimum total exposure of ~102 Ms (choosing the minimum source exposure among those in a field, for each field). The catalogue mostly includes sources detected in the second processing stage.

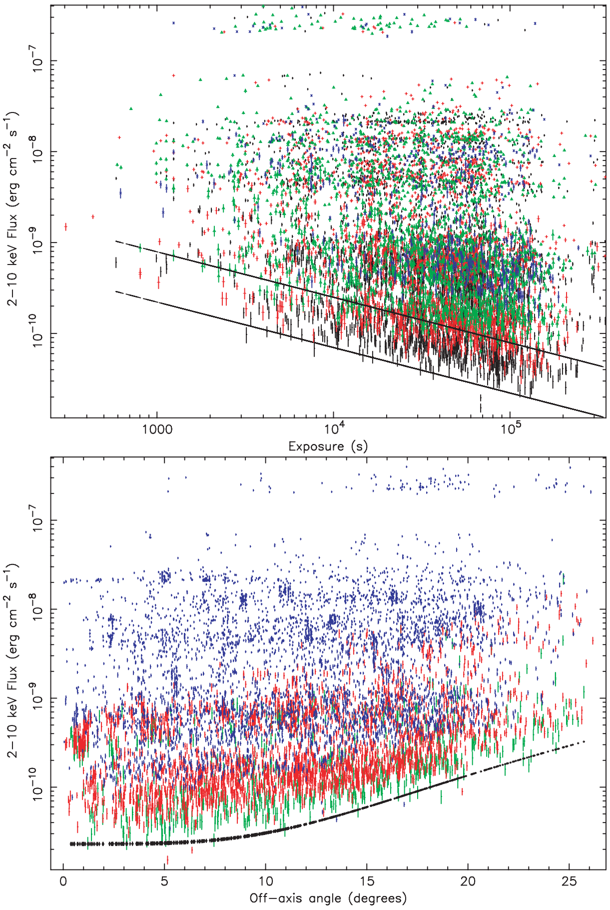

Fig. 7. The 2–10 keV flux as a function of the exposure (*top panel*) of the final sample of detections. The dashed lines on the bottom part of the plot show the limiting sensitivity model (proportional to the exposure square root) for fields out of the Galactic Plane (*the lowest*) and the GC ones. In the bottom panel the same flux vs the off-axis angle. The dashed curve on the bottom part of the plot shows a model of the limiting sensitivity as a function of the off-axis angle.

The 2–10 keV flux vs the exposures for all the detections in the sample in Fig. 7 (top panel) shows up the flux limit reached (~3×10^{-11} erg cm^{-2} s^{-1}) and the limiting sensitivity of the catalogue as a function of the exposure which follows the usual relation $F_x^{\text{limit.}}$(2–10 keV)$\simeq c/T^{1/2}$, where the constant c is

$$c \simeq \begin{cases} 7 \times 10^{-9}\ \mathrm{erg\,cm^{-2}\,s^{-1/2}} & \text{for } |b| > 30^\circ \\ 3 \times 10^{-8}\ \mathrm{erg\,cm^{-2}\,s^{-1/2}} & \text{for GC region.} \end{cases} \tag{1}$$

These numbers are consistent with the predictions in Jager et al. (1997). It should be noted that for GC fields the sensitivity reaches a limit at about 100 ks of net exposure due to the above mentioned imperfect imaging. In the bottom panel of the same figure the 2–10 keV flux as a function of the off-axis-angle

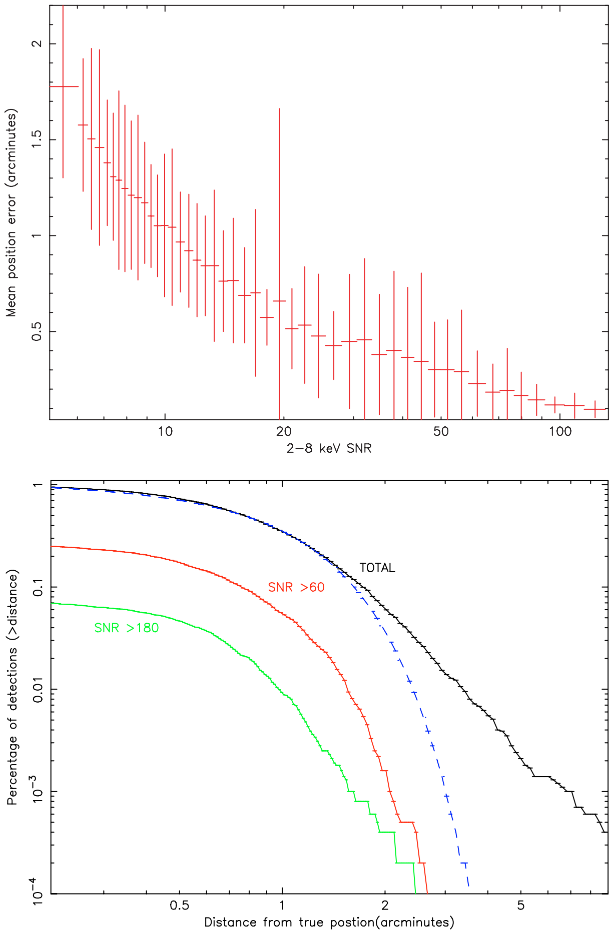

Fig. 8. Positional 99% error radius (in arcmin) as a function of the *SNR* (*top panel*), where each data point represents the average over 150 source positions and the standard deviation with respect to that average. In the bottom panel the cumulative distribution of the distances between measured positions and those in the reference catalogue (in arcminutes) for all the detections (upper curve) and for detections with *SNR* > 60 and *SNR* > 180. The radii including 99% of the detections are ~3.3′, 1.87′ and 1.78′ respectively. The dashed curve is the cumulative Gaussian component of the fit model applied to the upper curve, which represent the expected model for bright sources.

is given. An empirical model for the WFC limiting sensitivity, $F_x^{\text{limit.}}(2\text{–}10\,\text{keV}) \simeq (9.5\times10^{-16} \times R^{3.9}+2.3\times10^{-11})\,\text{erg}\,\text{cm}^{-2}\,\text{s}^{-1}\,\text{deg}^{-1}$, where R is the off-axis angle, has been evaluated for high galactic latitude fields.

The location accuracy reached is shown in Fig. 8. Source location accuracy is known to depend on source *SNR* (in ’t Zand 1992), so we plot the binned detection mean 99% position errors as a function of the *SNR* (top panel). In each bin we calculate the error average value and its standard deviation over detections having similar *SNR*s. No systematic error appears at high *SNR*s. We show in the bottom panel the cumulative distributions of distances between measured and catalogued positions, for all the detections and for those with *SNR* > 60 and *SNR* > 180. Distances were obtained cross-correlating our list with the reference catalogue using a radius of 5′. We computed then radii including 99% of the detections for all the distributions obtaining 3.30′, 1.87′ and 1.78′ for the total sample and the two sub-samples at increasing *SNR* thresholds respectively. We fitted these curves with a power law plus cumulative Gaussian model to evaluate the 99% confidence level error radius on the Gaussian component, which is the expected distribution for bright “good” detections. The three curves illustrate how at higher *SNR* thresholds the distributions are better represented by the Gaussian component. The radii for the three Gaussian components are 1.78′, 1.61′ and 1.33′ respectively. This last value is consistent with what previously reported for bright sources (Piro et al. 1997; Heise et al. 1998). This minimum location accuracy value has been added in quadrature as a systematic error to the mean 99% position error for each detection. The total position error computed for the maximum *SNR* detection of each source is reported in Table 3.

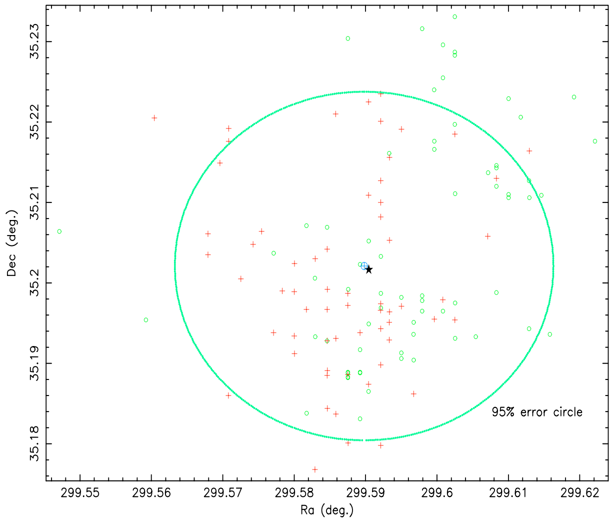

Fig. 9. The positions of all Cyg X-1 detections in equatorial coordinates. Crosses correspond to WFC unit 1, circles to unit 2, while the star corresponds to the Cyg X-1 reference catalogue position, RA = 299.5904, Dec = 35.2016 and the encircled cross to the best fit position, RA = 99.5898, Dec = 35.2021. The thick circle of radius ~1.6′ represents the 95% confidence level centered on the Gaussian model best fit position.

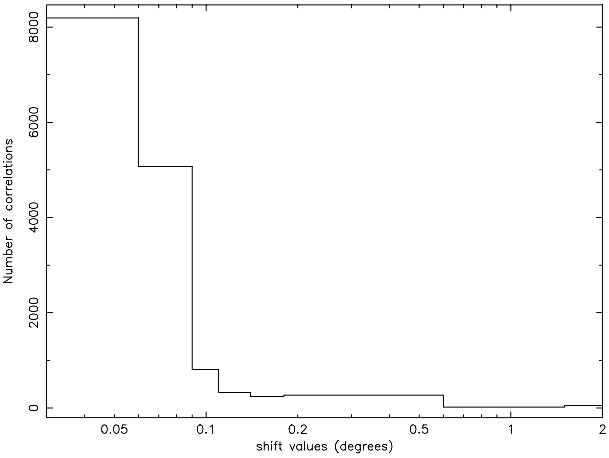

Fig. 10. Spurious matches in the cross-correlation of the *Beppo*SAX WFC catalogue with the reference catalogue with a radius of 5′ for “shift” values from 0° to 2°.

As an example of the location accuracy for a bright source we show in Fig. 9 the positions of all Cyg X-1 detections in equatorial coordinates. We fitted the distribution of Cyg X-1 positions in both coordinates with a Gaussian model obtaining a best fit mean position, RA = 299.5898, Dec = 35.2021 (J2000) with a ~1.6′ 95% confidence level radius.

The chance coincidence probability of the correlation between WFC detections and the reference catalogue positions

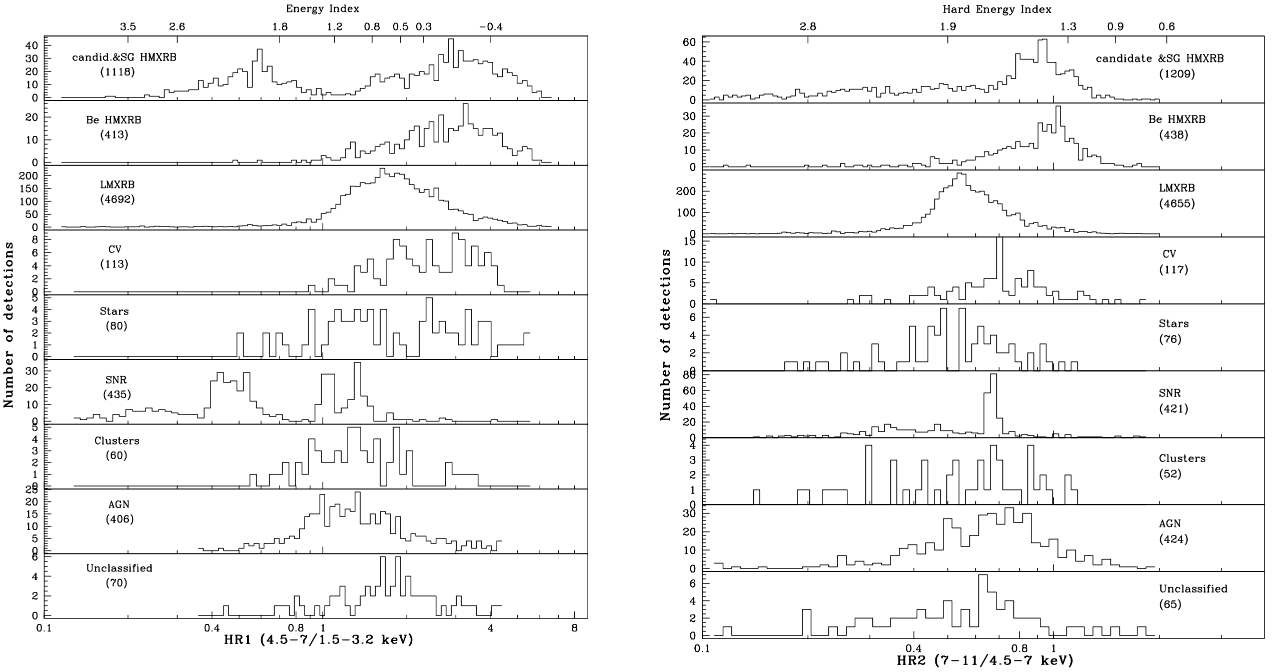

Fig. 11. The Hardness Ratio 1 (1.7–3.2/4.6–7.1 keV bands; *left panel*) distributions for each source class included in the catalogue. On the right the same per classes distributions of Hardness Ratio 2 (4.6–7.1/7.1–10.9 keV). Two corresponding energy indexes, evaluated assuming galactic absorption, are shown in the top scales of both panels. Numbers below each class label, in both panels, are the detections having non-null values of count rates and of energy indexes.

used in the source post-processing identification, can be evaluated by shifting the detection positions by various fixed amounts (between –10° and 10°) and executing again the cross-correlation with the same radius (see Fig. 10). The number of spurious matches for shift values greater than 0.16° is below ~3%.

We calculated two hardness ratios (HR1, HR2) using the 1.7–3.2, 4.6–7.1 and 7.1–10.9 keV bands for two sub-samples of 7439 and 7529 detections respectively, having non-zero values of count rates in these bands. The HR1 distribution for each individual source class included in the catalogue (see Table 2) is shown in Fig. 11. These histograms include HR1 values from all possible sources states, such as hard/soft states for LMXRBs and HMXRBs, all overlapped. In particular for Supergiant plus unclassified HMXRBs HR1 covers a very broad range of values with two peaks at ~0.6 and ~3.

The HR2 distributions for each source class are shown in the left panel of Fig. 11. In this case the plot for Supergiant HMXRBs class shows a prevailing harder peak at ~1, where the Be HMXRBs distribution peaks too. Two energy indexes were evaluated for both HRs assuming galactic absorption values for all sources. They are shown in the two panels of the figure as top scales. Their values range between –0.6 and 3.5 for that evaluated from HR1 and between 0.5 and 3.0 for the harder one.

5. Conclusions

We presented the complete post-mission catalogue of WFC X-ray sources detectable in complete observations, which includes 253 distinct objects. As shown in Table 2, these sources are mainly galactic (176 sources plus three candidate galactic transient sources, i.e. 71% of the total), while the smaller extra-galactic sample, 62 sources (25%), is mainly composed of AGN, 11 of which are BL Lacs (4.3%). The galactic sources are mostly LMXRBs (48%) while the HMXRBs (27%) include 13 classified Supergiant systems (7.3%) and 23 Be HMXRBs (13%). The 14 unclassified sources in Table 3, include two known sources, SAX J1428.6-5422 and SAX J1805.5-2031, and a new transient X-ray source, for which the WFC detections give the best localization so far. These are candidate transient galactic sources detected in outburst. Also included is a more uncertain candidate X-ray binary source (RX J0121.4-7258) and a possible BL Lac object (1RXS J205528.2-002123).

Most of the catalogue sources (83%) have a counterpart in the softer RASS catalogue (within 3′ radius). Moreover large fractions of sources have significant ($SNR \geq 7$) detections in the 2–5.5, 2–19 and 8–19 keV bands (219, 197 and 133 sources respectively), which have slightly lower percentages (71%, 70% and 64% respectively) of counterparts in the RASS. On the other hand the correlation with the harder INTEGRAL/IBIS Soft γ-ray catalogues (Bird et al. 2004, 2006 and 2007) give increasing percentages proportionally to the increasing INTEGRAL total exposure and sky coverage (29% with the first, 40% with the second and 53% with the most recent one, using the same 3′ radius). If we consider a sample of harder WFC sources (35%), detected ($SNR \geq 10$) in the 11–26 keV band, 78% resulted to have a counterpart in the last IBIS catalogue. The WFC catalogue thus includes sources detected up to 19 keV with still a good sensitivity (sources detected in this band have a 2–10 keV flux greater than about 3 mCrabs).

The cross-correlation with the RXTE "All Sky Monitor" source catalogue (available on-line[3]) finally gives the highest number of results (75%) among catalogues in hard X-ray bands. This result confirms the importance of the WFC source catalogue as a complementary reference catalogue for current and future hard X-ray missions, particularly in the 2–10 keV band.

---

[3] `http://xte.mit.edu/asmlc/asmcat.html`

Acknowledgements. The ASDC is supported by the Italian Space Agency (ASI). Part of this work benefitted of ASI grant I/024/05. FV, PG and PS thank S. Piranomonte for the help to the revision of source identifications and classes detected in the first data processing run. Authors thank all people of the WFC team at SRON, particularly G. Wiersma, for his collaboration and kindness.

References

Abell, G. O., Corwin, H. G. Jr., & Olowin, R. P. 1989, ApJS, 70, 1

Ables, J. G. 1968, PASA, 1, 172

Perlman, E. S., Horner, D. J., Jones, L. R., et al. 2002, ApJS, 140, 265

Bird, A. J., Barlow, E. J., Bassani, L., et al. 2004, ApJ, 607, L33

Bird, A. J., Barlow, E. J., Bassani, L., et al. 2006, ApJ, 636, 765

Bird, A. J., Malizia, A., Bazzano, A., et al. 2007, ApJS, 170, 175

Boella, G., Butler, R. C., Perola, G. C., et al. 1997, A&AS, 122, 299

Cornelisse, R., Heise, J., Kuulkers, E., Verbunt, F., & in 't Zand, J. J. M. 2000, A&A, 357, L21

Cornelisse, R., in 't Zand, J. J. M., Verbunt, F., et al. 2003, A&A, 405, 1033

Costa, E., Frontera, F., Heise, J., et al. 1997, Nature, 387, 783

Dicke, R. H. 1968, ApJ, 153, L101

Downes, R. A., & Shara, M. M. 1993, PASP, 105, 127

Fenimore, E. E., & Cannon, T. M. 1978, Appl. Opt., 17, 337

Giommi, P., Menna, M. T., & Padovani, P. 1999, MNRAS, 310, 465

Giommi, P., Perri, M., & Fiore, F. 2000, A&A, 362, 799

Giommi, P., Piranomonte, S., Perri, M., & Padovani, P. 2005, A&A, 434, 385

Hammersley, A. 1986, Ph.D. thesis, University of Birmingham

Hammersley, A., Ponman, T., & Skinner, G. K. 1992, Nucl. Instr. Meth. Phys. Res. A311, 585

Heise, J., in 't Zand, J. J. M., Muller, et al. 1998, in 4th Huntsville Symp. on Gamma-Ray Bursts, ed. C. Meegan, R. Preece, & T. Koshut (New York: AIP), AIP Conf. Proc., 428, 397

Huchra, J. P., Geller, M. J., Clemens, C. M., Tokarz, S. P., & Michel, A. 1992, Bull. Inf. Centre Données Stellaires, 41, 31

Jager, R., Mels, W., Brinkman, A., et al. 1997, A&AS, 125, 557

Kushino, A., Aoki, Y., Yamasaki, N. Y., et al. 2002, PASJ, 54, 327

Levine, A. M., Lang, F. L., Lewin, W. H. G., et al. 1984, ApJS, 54, 581

Liu Q. Z., van Paradijs, J., & van den Heuvel, E. P. J. 2000, A&AS, 147, 25

Liu Q. Z., van Paradijs, J., & van den Heuvel, E. P. J. 2001, A&AS, 368, 1021

Lumb, D. H., Warwick, R. S., Page, M., & De Luca, A. 2002, A&A, 389, 93

Markwardt, C. B., Barbier, L., Barthelmy, S., et al. 2005, A&AS, 207, 3801

Mels, W. A., Lowes, P., Buurmans, H. B., et al. 1988, Nucl. Instr. Meth. Phys. Res., A273, 689

Padovani, P., Giommi, P., & Fiore, F. 1997, Mem. Soc. Astron. It., 68, 147

Piro, L., Butler, R. C., Fiore, F., et al. 1997, Addendum to the SAX Observers' Handbook, on-line Techn. Report, `http://www.asdc.asi.it/bepposax/handbook/`

Revnivtsev, M. G., Sunyaev, R. A., Varshalovich, D. A., et al. 2004, PAZh, 30, 430

Strassmeier, K. G., Hall, D. S., Zeilik, M., et al. 1988, A&AS, 72, 291

Strassmeier, K. G., Hall, D. S., Fekel, F. C., & Scheck, M. 1993, A&AS, 100, 173

Sugizaki, M., Mitsuda, K., Kaneda, H., et al. 2001, ApJS, 134, 77

Ubertini, P., Bazzano, A., Cocchi, M., et al. 1999, ApJ, 514, L27

van Paradijs, J. 1995, in X-Ray Binaries, ed. W. H. G., Lewin , J., Van Paradijs, & E. P. J., Van Den Heuvel (Cambridge University Press)

Voges, W., Aschenbach, B., Boller, Th., et al. 1999, A&A, 349, 389

in 't Zand, J. J. M. 1992, Ph.D. thesis, University Utrecht

in 't Zand, J. J. M. 2001, in Exploring the gamma–ray universe, ed. A. Gimenez, V. Reglero, & C. Winkler, ESA Pub. Division, 163

in 't Zand, J. J. M., Verbunt, F., Heise, J., et al. 2004a, NuPhS, 132, 486

in 't Zand, J. J. M., Cornelisse, R., & Cumming, A. 2004b, A&A, 426, 257

in 't Zand, J. J. M., Cornelisse, R., Kuulkers, E., Verbunt, F., & Heise, J. 2004c, in X-Ray Timing 2003: Rossi and Beyond, ed. P. Kaaret, F. K. Lamb, & J. H. Swank (Melville, NY: AIP), AIP Conf. Proc., 714, 253

XMM-Newton Survey Science Centre, Consortium, 2003, yCat., 9037, 0

XMM-Newton Survey Science Centre, the Second XMM-Newton Serendipitous Source Pre-release Catalogue, 2006